


**Knee structure in the laser-intensity dependence of harmonic generation for graphene**Fulong Dong  and Jie Liu \**Graduate School, China Academy of Engineering Physics, Beijing 100193, China* (Received 22 March 2022; revised 18 August 2022; accepted 20 September 2022; published 4 October 2022)

We investigate the harmonic generation of graphene irradiated by linearly polarized lasers with intensities in a wide range from  $10^8$  W/cm<sup>2</sup> to  $10^{13}$  W/cm<sup>2</sup>. We find a striking knee structure in the laser intensity dependence of the harmonic yield, which consists of a perturbative region, followed by a plateau of saturated harmonic yield, and then a transition to nonperturbative growth. The knee structure is rather universal for the various harmonic orders and has been certified by two-band density-matrix equation calculations, as well as *ab initio* time-dependent density-functional theory calculations. Taking the third harmonic as an example and based on the two-band model, we reveal the underlying mechanisms: the perturbative region can be analytically depicted by perturbation theory, while the plateau of saturated harmonic yield and the transition to nonperturbative growth are caused by destructive and constructive quantum interference of harmonics generated by the electrons corresponding to the lattice momenta around Dirac points and  $M$  points in the Brillouin zone, respectively. In particular, we find that tuning the Fermi energy can effectively alter the knee structure, while the profile of the knee structure is not sensitive to temperature. Our calculations of the third-order harmonic versus tuned Fermi energy are compared with recent experiments, showing good agreement. Our predicted knee structure and its associated properties are observable with the current experimental techniques.

DOI: [10.1103/PhysRevA.106.043103](https://doi.org/10.1103/PhysRevA.106.043103)**I. INTRODUCTION**

With the rapid development of laser technology, high-order harmonic generation from the gases of atoms and molecules has been widely studied over the past several decades [1–4], leading to the birth of a new branch of physics, namely, attosecond science [5]. More recently, much attention has been given to harmonic generation in solid materials [6,7] due to the possibility of probing the electronic band structure [8,9] and obtaining coherent and bright attosecond pulses [6,10].

Graphene is a simple but specific two-dimensional material, containing only two carbon atoms per unit cell and the atoms are orderly arranged in a periodic hexagonal lattice. It has important applications because of its unusual optical properties [11]. Harmonic generation in graphene has attracted much attention experimentally [12,13] and theoretically [14,15]. The harmonic generation of graphene is found to be enhanced by elliptically polarized light [12,16–18], in contrast to the atomic cases. The harmonic ellipticity from graphene irradiated by elliptically [14,19] and linearly [19,20] polarized lasers has also been studied and apparent elliptic ninth harmonic emission has been observed and thoroughly investigated under a linearly polarized laser. In addition, the harmonic generation in bilayer and twisted bilayer graphene has also been studied [21,22].

In this work, we attempt to investigate the laser intensity dependence of harmonic yields in graphene. Note that in the situations of atoms and molecules, the issues associated with laser intensity dependence have been extensively addressed

for single and double ionization [23–27], as well as high-order harmonic generation [28,29]. Atomic or molecular ionization is found to transition from multiphoton ionization to above-threshold ionization, tunnel ionization, and finally overbarrier ionization with increasing laser intensity [30]. Additionally, the high-order harmonic yield and “cutoff” of the harmonic photon energy are dramatically altered by the laser intensity. In contrast to atomic and molecular systems, the harmonic in graphene is generated by the sum current of the electrons with various lattice momenta in the Brillouin zone. The quantum interference between the harmonics generated by different electrons will play an important role in harmonic generation. Obviously, the laser intensity will affect the yields and especially the phases of the harmonics generated by these electrons, which are therefore expected to alter the structure in the profile of the laser intensity dependence of the harmonic yields in graphene. Motivated by this consideration, in this paper, we calculate the harmonic yield of graphene for a wide range of laser intensities from  $10^8$  W/cm<sup>2</sup> to  $10^{13}$  W/cm<sup>2</sup> using the two-band density-matrix equations and time-dependent density-functional theory. The simulation results demonstrate a striking knee structure that consists of a perturbative region, then a plateau of saturated harmonic yield, and a transition to nonperturbative growth. The underlying mechanisms are analyzed. In particular, we find that tuning the Fermi energy can effectively alter the knee structure, while the profile of the knee structure is not sensitive to temperature.

This paper is organized as follows. We describe our calculation methods for the two-band density-matrix equations in the velocity gauge and time-dependent density-functional theory in Sec. II A and Sec. II B, respectively. Section III A

\*jliu@gascaep.ac.cn

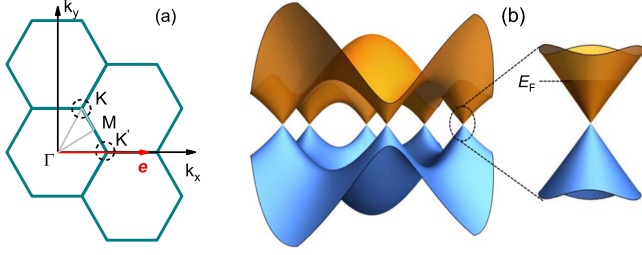


FIG. 1. (a) Brillouin zone of the reciprocal lattice of graphene. Points  $K$  and  $K'$  are two degenerate Dirac points and the red arrow indicates the polarization direction of the electric field. (b) Dispersion relation of valence and conduction bands of graphene under the nearest-neighbor tight-binding approximation.  $E_F$  is the Fermi energy of doped graphene.

presents our main calculated results and the mechanisms of the knee structure are discussed in Sec. III B. We also discuss the effects of finite temperature and Fermi energy tuning on the knee structure in Sec. III C. Finally, Sec. IV presents our conclusion. Throughout the paper atomic units are used if not specified.

## II. MODEL

### A. Two-band density-matrix equations

Graphene is a two-dimensional single layer of carbon atoms arranged in a honeycomb lattice [11,31] and its reciprocal space structure is a hexagonal lattice structure, as shown in Fig. 1(a). The tight-binding Hamiltonian  $H_0$  for electrons in graphene considering that electrons can only hop to nearest-neighbor atoms has the form

$$H_0 = \begin{pmatrix} 0 & \gamma_0 f(\mathbf{k}) \\ \gamma_0 f^*(\mathbf{k}) & 0 \end{pmatrix}, \quad (1)$$

where  $\mathbf{k}$  is the lattice momentum. In our calculation,  $\gamma_0 = 0.1$  a.u. is the nearest-neighbor hopping energy and  $f(\mathbf{k}) = e^{ik_y d} + 2 \cos(\sqrt{3}k_x d/2) e^{-ik_y d/2}$ , with a carbon-carbon bond length of  $d = 1.42$  Å ( $\approx 2.684$  a.u.). Diagonalization of the  $H_0$  matrix can yield energy eigenvalues, which describe the conduction ( $c$ ) and valence ( $v$ ) bands  $E_c(\mathbf{k}) = -E_v(\mathbf{k}) = \gamma_0 |f(\mathbf{k})| = \gamma_0 \sqrt{1 + 4 \cos^2(\sqrt{3}k_x d/2) + 4 \cos(\sqrt{3}k_x d/2) \cdot \cos(3k_y d/2)}$ .

Of particular importance for the physics of graphene are the two points  $K$  and  $K'$  at the corners of the graphene Brillouin zone. Their positions in momentum space are given by  $K = (\frac{2\pi}{3\sqrt{3}d}, \frac{2\pi}{3d})$  and  $K' = (\frac{4\pi}{3\sqrt{3}d}, 0)$ , as shown in Fig. 1(a). Figure 1(b) exhibits the electronic dispersion in the honeycomb lattice, where  $E_F$  is the Fermi energy of doped graphene.

We simulate the laser-graphene interaction by the two-band density-matrix equations (TBDMs) in the velocity gauge. Within the dipole approximation, they read

$$\begin{aligned} i \frac{\partial}{\partial t} \rho_{mn}(\mathbf{k}, t) &= [E_m(\mathbf{k}) - E_n(\mathbf{k})] \rho_{mn}(\mathbf{k}, t) \\ &+ \mathbf{A}(t) \cdot [\hat{\mathbf{p}}(\mathbf{k}), \hat{\rho}]_{mn} - i \Gamma_i \rho_{mn}(\mathbf{k}, t) (1 - \delta_{mn}) \\ &- i \Gamma_e [\rho_{mi}(\mathbf{k}, t) - \rho_{mi}(\mathbf{k}, t=0)] \delta_{mn}, \end{aligned} \quad (2)$$

where  $\hat{\rho}$  is the density matrix comprising elements  $\rho_{mn} = \langle m, \mathbf{k} | \rho | n, \mathbf{k} \rangle$ , where  $m$  and  $n$  represent the valence or conduction band.  $\Gamma_i$  and  $\Gamma_e$ , independent of  $\mathbf{k}$ , are relaxation parameters. The momentum matrix  $\hat{\mathbf{p}}(\mathbf{k})$  consists of the intraband dipole elements  $\mathbf{p}_{cc}(\mathbf{k}) = \nabla_{\mathbf{k}} E_c(\mathbf{k}) = -\mathbf{p}_{vv}(\mathbf{k})$  and the interband dipole elements  $\mathbf{p}_{cv}(\mathbf{k}) = i[E_c(\mathbf{k}) - E_v(\mathbf{k})] \mathbf{D}_{cv}(\mathbf{k}) = -\mathbf{p}_{vc}(\mathbf{k})$ , where  $\mathbf{D}_{cv}(\mathbf{k}) = i \langle u_{c,\mathbf{k}}(\mathbf{r}) | \nabla_{\mathbf{k}} | u_{v,\mathbf{k}}(\mathbf{r}) \rangle$  and  $u_{c,\mathbf{k}}(\mathbf{r})$  [ $u_{v,\mathbf{k}}(\mathbf{r})$ ] is the periodic part of the Bloch wave function for the conduction (valence) band of graphene with crystal momentum  $\mathbf{k}$  [32,33].

$\mathbf{A}(t) = A_0 f(t) \sin(\omega_0 t) \mathbf{e}$  is the vector potential of the laser field and  $f(t)$  is an eight-cycle sine square envelope.  $A_0$  is the amplitude of the vector potential and  $\omega_0$  is the frequency of the laser field corresponding to wavelength  $\lambda = 5500$  nm.  $\mathbf{e}$  is the unit vector along the laser polarization direction, as indicated by the red arrow in Fig. 1(a).

At the initial moment  $t = 0$ , the density operator  $\rho_{mn}(\mathbf{k}, t = 0)$  is equal to  $\delta_{mn} f_{m\mathbf{k}}$ , which characterizes the equilibrium occupation of single-particle states at finite temperature  $T$  and Fermi energy  $E_F$  [34], where

$$f_{m\mathbf{k}} = [1 + e^{(E_m(\mathbf{k}) - E_F)/(k_B T)}]^{-1} \quad (3)$$

is the Fermi-Dirac distribution with Boltzmann's constant  $k_B$ .

Next, the total current can be evaluated by

$$\mathbf{j}_{\text{tot}}(t) = \sum_{\mathbf{k} \in \text{BZ}} \mathbf{j}(\mathbf{k}, t) \quad (4)$$

and

$$\mathbf{j}(\mathbf{k}, t) = \text{Tr}\{\hat{\rho}[\hat{\mathbf{p}}(\mathbf{k}) + \mathbf{A}(t)]\} = \sum_{mn} \mathbf{p}_{mn}(\mathbf{k}) \rho_{nm}(\mathbf{k}, t) + \mathbf{A}(t), \quad (5)$$

where Tr denotes the trace and BZ denotes the first Brillouin zone.

The total yield of  $\omega$ -frequency emission can be evaluated using

$$H_{\text{tot}}(\omega) = \omega^2 |F_{\text{tot}}(\omega)|^2, \quad (6)$$

in which

$$F_{\text{tot}}(\omega) = \mathcal{T}_F[\mathbf{e} \cdot \mathbf{j}_{\text{tot}}(t)] = \int_{-\infty}^{\infty} \mathbf{e} \cdot \mathbf{j}_{\text{tot}}(t) e^{-i\omega t} dt, \quad (7)$$

where  $\mathcal{T}_F$  denotes the Fourier transform.

### B. Time-dependent density-functional theory

Since our density-matrix equations only consider two energy bands under the tight-binding approximation, we check our main results with time-dependent density-functional theory (TDDFT) [35]. Within the TDDFT framework, the evolution of the wave function is computed by propagating the Kohn-Sham equations [36–38]:

$$i \frac{\partial}{\partial t} \psi_i(\mathbf{r}, t) = \hat{H}_{\text{KS}}(\mathbf{r}, t) \psi_i(\mathbf{r}, t), \quad (8)$$

where  $\psi_i(\mathbf{r}, t)$  is the wave function of an electron with the index  $i$ .  $\hat{H}_{\text{KS}}$  is the Kohn-Sham Hamiltonian in the velocity gauge given by

$$\hat{H}_{\text{KS}}(\mathbf{r}, t) = \frac{1}{2} [\hat{\mathbf{p}} + \mathbf{A}(t)]^2 + V_{\text{KS}}(\mathbf{r}, t), \quad (9)$$

where  $V_{KS}(\mathbf{r}, t) = V(\mathbf{r}, t) + V_{\text{Hartree}}[\mathbf{n}](\mathbf{r}, t) + V_{xc}[\mathbf{n}](\mathbf{r}, t)$  is the Kohn-Sham potential and  $V_{\text{Hartree}}[\mathbf{n}](\mathbf{r}, t)$  is the Hartree potential.  $\mathbf{n}(\mathbf{r}, t) = \sum_i |\psi_i(\mathbf{r}, t)|^2$  is the electron density.  $V(\mathbf{r}, t)$  represents the interaction between four valence electrons and the ionic core and is modeled by norm-conserving pseudopotentials.  $V_{xc}[\mathbf{n}](\mathbf{r}, t)$  is the exchange-correlation potential. Here, we apply the generalized gradient approximation in the Perdew-Burke-Ernzerhof parametrization, which accounts for the short-range correlations and neglects some long-range processes, such as excitonic and Auger effects involving the interband transitions [39–41].

In the calculation of the harmonic generation in graphene, a  $60 \times 60 \times 1$   $k$ -point mesh is used to sample the Brillouin zone and the real-space spacing is  $0.2 \text{ \AA}$  ( $\approx 0.378$  a.u.). The parameters of the vector potential  $\mathbf{A}(t)$  of the laser field are the same as those used in the two-band density-matrix equations. The OCTOPUS package [42,43] is employed to perform the simulations.

We compute the total electronic current  $\mathbf{j}(\mathbf{r}, t)$  from time-evolved wave functions. The harmonic yield can be evaluated using  $H_{\text{tot}}(\omega) = \omega^2 |F_{\text{tot}}(\omega)|^2$ , in which  $F_{\text{tot}}(\omega) = \mathcal{T}_F[\mathbf{e} \cdot \int_{\Omega} d^3 \mathbf{r} \mathbf{j}(\mathbf{r}, t)]$ , where  $\Omega$  is the volume of the physical system.

### III. KNEE STRUCTURE IN LASER INTENSITY-DEPENDENT HARMONIC GENERATION

#### A. Main results

In Fig. 2(a), we demonstrate the dependence of the harmonic yield calculated by the TBDMEs in the velocity gauge on the laser intensity over a wide range from  $10^8 \text{ W/cm}^2$  to  $10^{13} \text{ W/cm}^2$  for the third- to ninth-order harmonics. The results indicate that for each harmonic order, as the laser intensity increases, the harmonic yield first linearly increases, then saturates, and finally nonlinearly increases. The profiles exhibit visible knee structures for harmonics up to the ninth order. To verify the results calculated by TBDMEs in the velocity gauge, we perform TDDFT calculations and the TBDME simulation of the length gauge (see Appendix A for details). The results are shown in Figs. 2(b) and 2(c), which exhibit knee structures analogous to those in Fig. 2(a). In Figs. 2(a)–2(c), the dashed lines show that the  $n$ th-order harmonic yield  $H_{\text{tot}}(n\omega_0)$  is proportional to the  $n$ th power of the laser intensity  $I$ , namely,  $H_{\text{tot}}(n\omega_0) \propto I^n$ , as predicted by perturbation theory.

Figure 2(d) compares the laser intensity dependence of the third harmonic yield calculated by the TBDME simulations of the length gauge and velocity gauge and TDDFT, indicating that apparent knee structures emerge for the three methods. The knee structure consists of a perturbative region, plateau region, and nonperturbative growth region that correspond to laser intensities ranging from  $1 \times 10^8 \text{ W/cm}^2$  to  $1 \times 10^9 \text{ W/cm}^2$ ,  $1 \times 10^9 \text{ W/cm}^2$  to  $2 \times 10^{10} \text{ W/cm}^2$ , and  $2 \times 10^{10} \text{ W/cm}^2$  to  $1 \times 10^{13} \text{ W/cm}^2$ , respectively. Quantitatively, there are some deviations between the results of the TBDMEs in the length gauge and velocity gauge, especially in the nonperturbative growth region. These deviations might be partly due to the velocity gauge requiring the solution of dynamics equations on a basis including many virtual states (conduction and valence bands), which are not physically

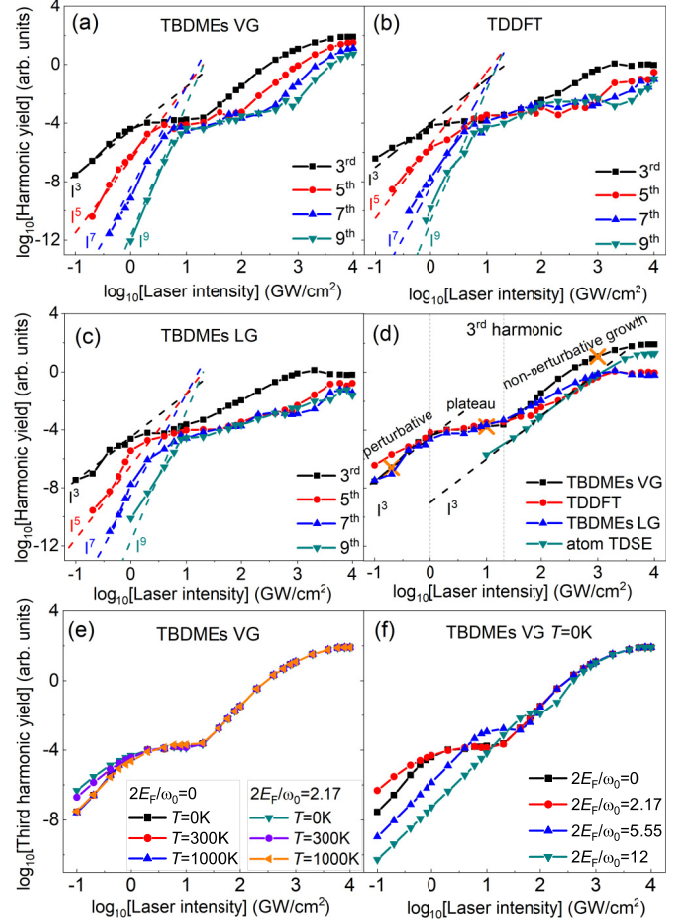


FIG. 2. Laser intensity dependence of the harmonic yield calculated by the TBDMEs in the velocity gauge (VG) (a), TDDFT (b), and TBDMEs in the length gauge (LG) (c). (d) Comparison of the third harmonic yields of graphene calculated by the TBDMEs and TDDFT with that of the model atom calculated by the time-dependent Schrödinger equation (TDSE). The three orange crosses mark the laser intensities  $I = 2 \times 10^8 \text{ W/cm}^2$ ,  $1 \times 10^{10} \text{ W/cm}^2$ , and  $1 \times 10^{12} \text{ W/cm}^2$ . In panels (a), (b), (c), and (d), the dashed lines show the  $I^n$  dependence for the  $n$ th harmonic. (e) Effects of finite temperatures on the knee structure of the third harmonic when the Fermi energy is tuned to  $E_F = 0$  or  $2E_F = 2.17\omega_0$ . (f) Effects of Fermi energy tuning on the knee structure of the third harmonic when the temperature is zero. Here, for the TBDMEs of the velocity and length gauges, all relaxation parameters are set to 0 and the laser wavelength is 5500 nm.

occupied [44,45]. However, because the velocity gauge can basically characterize the profile of the knee structure and has the advantage that the transitions induced by the external field formally preserve the crystal momentum [46], we prefer to exploit the velocity gauge to discuss the mechanism of the knee structure. In Appendix A, we have made some comparative calculations showing that the main results of the TBDMEs in the velocity gauge can be well reproduced by the TBDMEs in the length gauge.

In Fig. 2(d), we also show the third harmonic yields of the model atom. The ionization potential of the model atom is 0.1 a.u. [47,48]. In contrast to the results of graphene, the third

harmonic yield of the model atom increases monotonically from  $1 \times 10^{10}$  W/cm<sup>2</sup> to  $1 \times 10^{12}$  W/cm<sup>2</sup>. As the laser intensity increases further, the increasing trend of the harmonic yield is suppressed. No apparent knee structure is observed. This phenomenon of atomic harmonic generation has also been observed in previous experiments [28,29].

Note that the above interesting knee structure did not appear in previous works that investigated the laser intensity dependence of the harmonic yield for crystalline solids and some two-dimensional materials [9,12,49–51] because their calculations were only implemented for a narrow range of laser intensities. In this work, we extend our calculations to a wide range of laser intensities from  $1 \times 10^8$  W/cm<sup>2</sup> to  $1 \times 10^{13}$  W/cm<sup>2</sup>. In a recent experiment [12], a laser with an intensity of  $1.7 \times 10^{12}$  W/cm<sup>2</sup> and a duration of approximately 95 fs was used to irradiate graphene. In the experiment of Ref. [52], the authors established that graphene has a higher power damage threshold of  $3 \times 10^{12}$  W/cm<sup>2</sup> for a 50 fs laser pulse. In the theoretical work of Ref. [53], the energy damage threshold is estimated as 0.29 J/cm<sup>2</sup>. In the present work, the duration time of the laser pulse is approximately 73 fs (full width at half maximum of the laser) and the power damage threshold is approximately  $4 \times 10^{12}$  W/cm<sup>2</sup>, which corresponds to the energy damage of 0.29 J/cm<sup>2</sup>. The laser intensities in the nonperturbative growth region might be slightly above the power damage threshold, while the knee structure regime is well below the threshold and therefore can be experimentally accessed.

Gate tuning of the Fermi energy allows control of the optical properties, leading to many promising applications in optoelectronics and photonics [54,55]. Additionally, the effects of finite temperature on the harmonic yield are often taken into account [56–58]. Here, we also attempt to consider the influence of the Fermi energy and finite temperature on the knee structure. Figure 2(e) shows that the profile of the knee structure does not change with temperature when the Fermi energy is equal to 0. When the Fermi energy is tuned to  $2E_F = 2.17\omega_0$ , the perturbative region of the knee structure is weakly influenced by temperature. In contrast, tuning the Fermi energy has a substantial effect on this structure [see Fig. 2(f)] when the temperature is set to zero. When the Fermi energy is tuned to  $2E_F = 2.17\omega_0$ , compared with  $E_F = 0$ , the harmonic yield in the perturbative region markedly increases. When the Fermi energy is tuned to  $2E_F = 5.55\omega_0$ , the harmonic yield in the perturbative region is suppressed and that in the plateau region is enhanced. Finally, the knee structure almost disappears when the Fermi energy is further increased to  $2E_F = 12\omega_0$ . The increase in  $E_F$  only changes the transition processes of the  $\mathbf{k}$  space through Pauli blocking, which can prevent multiphoton transitions and effectively alter the knee structure. Nevertheless, the profile of the knee structure is not sensitive to temperature.

## B. Mechanism analysis at zero temperature

Taking the third harmonic as an example and based on the two-band model, we discuss the mechanisms for the observed harmonic behavior. To simplify formulas, we hat tildes on the physical quantities associated with the third harmonic emission.

### 1. Perturbative region

The total yield of the third harmonic  $\tilde{H}_{\text{tot}} \equiv H_{\text{tot}}(3\omega_0)$  is the coherent sum over the harmonic amplitudes generated by the Bloch electrons, according to Eqs. (6) and (7):

$$\tilde{H}_{\text{tot}} = \left| \sum_{\mathbf{k} \in \text{BZ}} [\sqrt{\tilde{H}(\mathbf{k})} e^{i\tilde{\phi}(\mathbf{k})}] \right|^2, \quad (10)$$

where  $\tilde{H}(\mathbf{k})$  is the third harmonic yield of the Bloch electron with lattice momentum  $\mathbf{k}$ , which is expressed as  $\tilde{H}(\mathbf{k}) = (3\omega_0)^2 |\tilde{F}(\mathbf{k})|^2$ , where  $\tilde{F}(\mathbf{k}) = \int_{-\infty}^{\infty} \mathbf{e} \cdot \mathbf{j}(\mathbf{k}, t) e^{-i3\omega_0 t} dt$ .  $\tilde{\phi}(\mathbf{k}) = \arg[\tilde{F}(\mathbf{k})] \in [-\pi, \pi)$  is the corresponding harmonic phase, which is calculated by considering  $\tan[\tilde{\phi}(\mathbf{k})] = \text{Im}[\tilde{F}(\mathbf{k})] / \text{Re}[\tilde{F}(\mathbf{k})]$ , as well as the signs of  $\text{Im}[\tilde{F}(\mathbf{k})]$  and  $\text{Re}[\tilde{F}(\mathbf{k})]$ .

For a laser intensity of  $2 \times 10^8$  W/cm<sup>2</sup> of the perturbative region, we numerically calculate the yields [Figs. 3(a) and 3(c)] and phases [Figs. 3(b) and 3(d)] of the harmonic, which are generated by the electrons corresponding to lattice momenta  $\mathbf{k}$  around  $K$  [Figs. 3(a) and 3(b)] and  $K'$  [Figs. 3(c) and 3(d)], as marked by the two dashed circles in Fig. 1(a). From Figs. 3(a) to 3(d), the labels of “1,” “2,” and “3” represent the ring positions corresponding to band frequency differences of  $\omega_{cv} = E_{cv}(\mathbf{k}) = E_c(\mathbf{k}) - E_v(\mathbf{k}) = 1\omega_0$ ,  $2\omega_0$ , and  $3\omega_0$ , respectively, where  $E_{cv}(\mathbf{k})$  is the band energy difference between the conduction and valence bands. As shown in Figs. 3(a) and 3(c), the third harmonic yield is mainly contributed by the electrons with  $E_{cv}(\mathbf{k}) = \omega_{cv} = 2\omega_0$  and  $E_{cv}(\mathbf{k}) = \omega_{cv} = 3\omega_0$ . In Figs. 3(b) and 3(d), we show the distributions of harmonic phases  $\tilde{\phi}(\mathbf{k})$ , which are not disordered. Centered on the  $K$  and  $K'$  points and along the radial direction, there are some apparent  $\pm\pi$ -phase changes at  $\omega_{cv} = 1\omega_0$ ,  $2\omega_0$ , and  $3\omega_0$ , exhibiting some ring structures that depend on  $\omega_{cv}$  in Figs. 3(b) and 3(d). These results indicate that we can evaluate the third harmonic yields and phases that are functions of the band frequency difference  $\omega_{cv}$ .

According to Eqs. (6) and (7), we can also express the total yield of the third harmonic  $\tilde{H}_{\text{tot}}$  as the coherent sum over harmonic amplitudes generated by the Bloch electrons with different band frequency differences, i.e.,

$$\tilde{H}_{\text{tot}} = \left| \sum_{\omega_{cv}} [\sqrt{\tilde{H}(\omega_{cv})} e^{i\tilde{\phi}(\omega_{cv})}] \right|^2, \quad (11)$$

with the amplitude of  $\tilde{H}(\omega_{cv}) = (3\omega_0)^2 |\tilde{F}(\omega_{cv})|^2$  and the phase of  $\tilde{\phi}(\omega_{cv}) = \arg[\tilde{F}(\omega_{cv})] \in [-\pi, \pi)$ , in which  $\tilde{F}(\omega_{cv}) = \int_{-\infty}^{\infty} \mathbf{e} \cdot \mathbf{j}(\omega_{cv}, t) e^{-i3\omega_0 t} dt$  and the currents  $\mathbf{j}(\omega_{cv}, t)$  are defined by

$$\mathbf{j}(\omega_{cv}, t) = \sum_{\mathbf{k} \in E_{cv}(\mathbf{k})=\omega_{cv}} \mathbf{j}(\mathbf{k}, t). \quad (12)$$

Namely, the current  $\mathbf{j}(\omega_{cv}, t)$  is the sum of the currents  $\mathbf{j}(\mathbf{k}, t)$  generated by electrons whose lattice momenta  $\mathbf{k}$  satisfy  $E_{cv}(\mathbf{k}) = \omega_{cv}$ . Note that we do not execute any kind of normalization here and that

$$\sqrt{\tilde{H}(\omega_{cv})} e^{i\tilde{\phi}(\omega_{cv})} = \sum_{\mathbf{k} \in E_{cv}(\mathbf{k})=\omega_{cv}} \sqrt{\tilde{H}(\mathbf{k})} e^{i\tilde{\phi}(\mathbf{k})}. \quad (13)$$

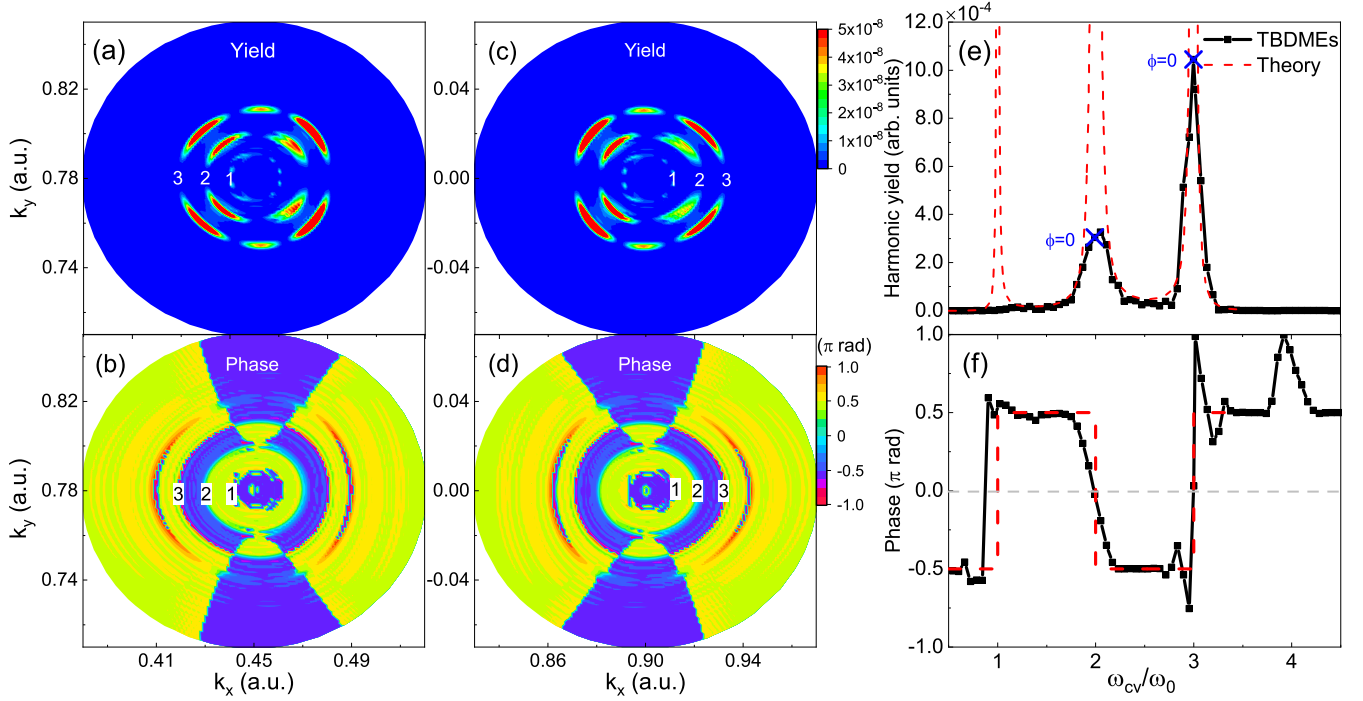


FIG. 3. Harmonic yield  $\tilde{H}(\mathbf{k})$  [(a) and (c)] and phase  $\tilde{\phi}(\mathbf{k})$  [(b) and (d)] for the  $\mathbf{k}$  points around the  $K$  [(a) and (b)] and  $K'$  [(c) and (d)] points of the Brillouin zone, as demonstrated by the two dashed circles in Fig. 1(a). The positions where the band frequency difference is  $\omega_{cv} = 1\omega_0$ ,  $2\omega_0$ , and  $3\omega_0$  are labeled by “1,” “2,” and “3,” respectively. In panels (e) and (f), the black square curves are the yield  $\tilde{H}(\omega_{cv})$  and phase  $\tilde{\phi}(\omega_{cv})$ , respectively. The corresponding red dashed lines are evaluated by Eqs. (B6) and (B7) of perturbation theory. In (e), the blue crosses label the harmonic yields at  $\omega_{cv} = 2\omega_0$  and  $\omega_{cv} = 3\omega_0$ , and the corresponding phases  $\tilde{\phi}(\omega_{cv})$  are appended. Note that the above numerical results are calculated by the TBDMEs of the velocity gauge with Fermi energy  $E_F = 0$  and temperature  $T = 0$  K for the laser intensity of  $2 \times 10^8$  W/cm<sup>2</sup> in the perturbative region.

The harmonic yield and phase as a function of the band frequency difference  $\omega_{cv}$  are shown in Figs. 3(e) and 3(f), respectively. In Fig. 3(e), our calculated results (black square curve) present two main harmonic yield peaks around  $\omega_{cv} = 2\omega_0$  and  $3\omega_0$ , which are consistent with the results of Figs. 3(a) and 3(c). At the band frequency differences of  $\omega_{cv} = 1\omega_0$ ,  $2\omega_0$ , and  $3\omega_0$ , we find some interesting phase changes in Fig. 3(f), which correspond to the ring structures in Figs. 3(b) and 3(d).

The phase changes at  $\omega_{cv} = 1\omega_0$ ,  $2\omega_0$ , and  $3\omega_0$  can be well understood by perturbation theory [34,59,60], which is presented in detail in Appendix B. The yield  $\tilde{H}(\omega_{cv})$  and phase  $\tilde{\phi}(\omega_{cv})$  (red dashed lines) calculated by Eqs. (B6) and (B7) are shown in Figs. 3(e) and 3(f), respectively (see Appendix B for the detailed derivations). The perturbation theory results qualitatively agree with the numerical results. We find that across each resonance peak at  $\omega_{cv} = 1\omega_0$ ,  $2\omega_0$ , or  $3\omega_0$ , there is a phase jump of  $-\pi$  or  $+\pi$ . According to Eq. (11), we see that the harmonic yields generated by the Bloch electrons around the resonance peaks cancel each other such that the total harmonic yield  $\tilde{H}_{\text{tot}}$  approximately equals the sum of  $\tilde{H}(\omega_{cv} = 2\omega_0) + \tilde{H}(\omega_{cv} = 3\omega_0)$ , considering that the phases at the resonance peaks are zero and  $\tilde{H}(\omega_{cv} = \omega_0)$  is small. According to Eq. (B6) in Appendix B, we have  $\tilde{H}(\omega_{cv} = 2\omega_0) + \tilde{H}(\omega_{cv} = 3\omega_0) \propto I^3$ , indicating that the third harmonic yield is proportional to the third power of the laser intensity.

## 2. Plateau region

In contrast to Figs. 3(a) and 3(c), we find that for  $1 \times 10^{10}$  W/cm<sup>2</sup> of the plateau region, the Bloch electrons with a wide range of momenta corresponding to more than eight resonance rings [i.e., band frequency differences of  $\omega_{cv} = q\omega_0$  ( $q = 1, 2, \dots, 8$ ) in Figs. 4(a) and 4(c)] can emit the third harmonic  $\tilde{H}(\mathbf{k})$ . Accordingly, the phase distribution also demonstrates some ring structures, as shown in Figs. 4(b) and 4(d). Note that for the intermediate laser field in the plateau region, the resonance peaks show some small shifts due to Stark effects.

Figures 4(e) and 4(f) show the harmonic yields  $\tilde{H}(\omega_{cv})$  and phases  $\tilde{\phi}(\omega_{cv})$  as a function of the band frequency difference  $\omega_{cv}$ . When the band frequency difference is below  $2.8\omega_0$ , the yields  $\tilde{H}(\omega_{cv})$  are small enough so that their contribution to the total harmonic yield  $\tilde{H}_{\text{tot}}$  can be ignored. In the band frequency difference range from  $2.8\omega_0$  to  $5.5\omega_0$ , there are two main yield peaks marked by black crosses. The corresponding phases are  $-0.53\pi$  and  $-0.47\pi$ , which are approximated to be  $-\pi/2$ . From  $5.5\omega_0$  to  $8\omega_0$ , there also exist two yield peaks labeled by the blue crosses and the corresponding phases are  $0.55\pi$  and  $0.66\pi$ , respectively, which are approximated to be  $\pi/2$ . According to Eq. (11), the  $\pi$ -phase difference can cause the destructive interference of the harmonic yields  $\tilde{H}(\omega_{cv})$ . This picture is maintained in the plateau region, which implies that with increasing laser intensities, the total harmonic yields might not increase like that in the perturbative region because

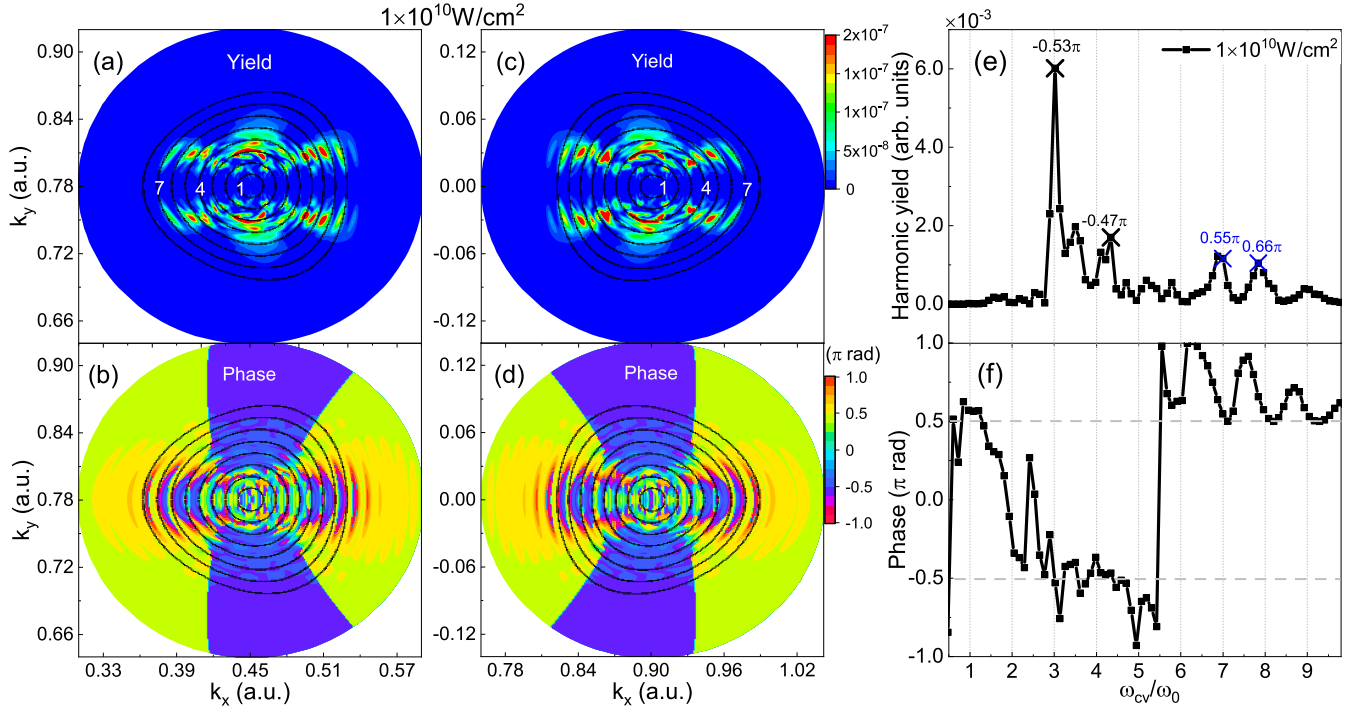


FIG. 4. Panels (a), (b), (c), and (d) are the same as those in Fig. 3, but the laser intensity is  $1 \times 10^{10}$  W/cm<sup>2</sup>, which is in the plateau region. (e) The yield  $\tilde{H}(\omega_{cv})$  and (f) phase  $\tilde{\phi}(\omega_{cv})$  numerically calculated by the TBDMEs of the velocity gauge for laser intensities of  $1 \times 10^{10}$  W/cm<sup>2</sup>. In (e), the crosses mark the harmonic yield peaks and the corresponding phases  $\tilde{\phi}(\omega_{cv})$  are appended.

of the destructive interference mechanism. This mechanism can be used to understand the striking plateau of saturated harmonic yield.

### 3. Nonperturbative growth region

For a laser intensity of  $1 \times 10^{12}$  W/cm<sup>2</sup> of the nonperturbative growth region, Figs. 5(a) and 5(b) present the harmonic yields  $\tilde{H}(\mathbf{k})$  and phases  $\tilde{\phi}(\mathbf{k})$  corresponding to all lattice momenta  $\mathbf{k}$  of the first Brillouin zone. In contrast to the perturbative and plateau regions, Fig. 5(a) shows that harmonic yields  $\tilde{H}(\mathbf{k})$  are mainly contributed by the lattice momenta near  $M$  points. Figures 5(c) and 5(d) exhibit the harmonic yield  $\tilde{H}(\omega_{cv})$  and phase  $\tilde{\phi}(\omega_{cv})$  as a function of the band frequency difference  $\omega_{cv}$ . The gray line in Fig. 5(c) is the density of states (DOS). Note that the orange hexagons in the left panels of Fig. 5 correspond to the band frequency difference of  $M$  points ( $\omega_{cv}^M \approx 24.1\omega_0$ ), which is also indicated by the orange vertical dashed line in the right panels. Moreover, we observe a  $\pi$ -phase jump at  $\omega_{cv}^{\text{jump}} \approx 33.7\omega_0$  indicated by the black vertical dashed line in the right panels, which corresponds to the black circle in Fig. 5(b).

In contrast to that of the perturbative and plateau regions, there is only one dominating peak in Fig. 5(c). Moreover, the formation of the peak is not due to multiphoton resonance (i.e.,  $\omega_{cv} = q\omega_0$ ), but arises from constructive quantum interference. On the one hand, as shown by the gray line in Fig. 5(c), the density of states is a maximum at the band frequency difference of  $\omega_{cv}^M$ , corresponding to  $M$  points of the Brillouin zone [11]. According to Eq. (13), this result implies that at  $\omega_{cv}^M$ , most electrons with  $\mathbf{k} \in E_{cv}(\mathbf{k}) = \omega_{cv}^M$  can contribute to  $\tilde{H}(\omega_{cv}^M)$ . On the other hand, by carefully

investigating the distributions of amplitudes and phases on the orange hexagons [i.e.,  $\mathbf{k} \in E_{cv}(\mathbf{k}) = \omega_{cv}^M$ ] in Figs. 5(a) and 5(b), one can find that for high yield  $\tilde{H}(\mathbf{k})$  located around  $M$  points, the corresponding phases  $\tilde{\phi}(\mathbf{k})$  are all  $-\pi/2$ .

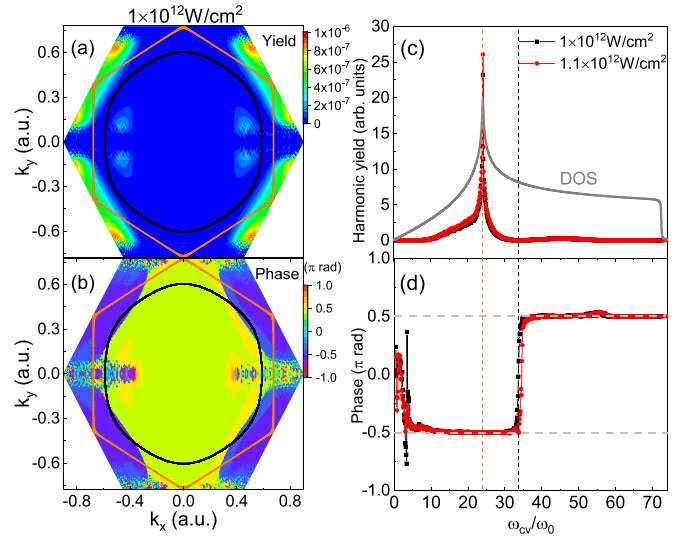


FIG. 5. (a) Harmonic yield  $\tilde{H}(\mathbf{k})$  and (b) phase  $\tilde{\phi}(\mathbf{k})$  generated by electrons corresponding to all  $\mathbf{k}$  points of the first Brillouin zone for the laser intensity of  $1 \times 10^{12}$  W/cm<sup>2</sup> in the nonperturbative growth region. (c) The yield  $\tilde{H}(\omega_{cv})$  and (d) phase  $\tilde{\phi}(\omega_{cv})$  for laser intensities of  $1 \times 10^{12}$  W/cm<sup>2</sup> and  $1.1 \times 10^{12}$  W/cm<sup>2</sup>. In panel (c), the gray line is the density of states (DOS).  $\omega_{cv}^M$  (or  $\omega_{cv}^{\text{jump}}$ ) corresponding to the orange hexagons (or black circles) in the left panels is indicated by the orange (or black) vertical dashed line in the right panels.

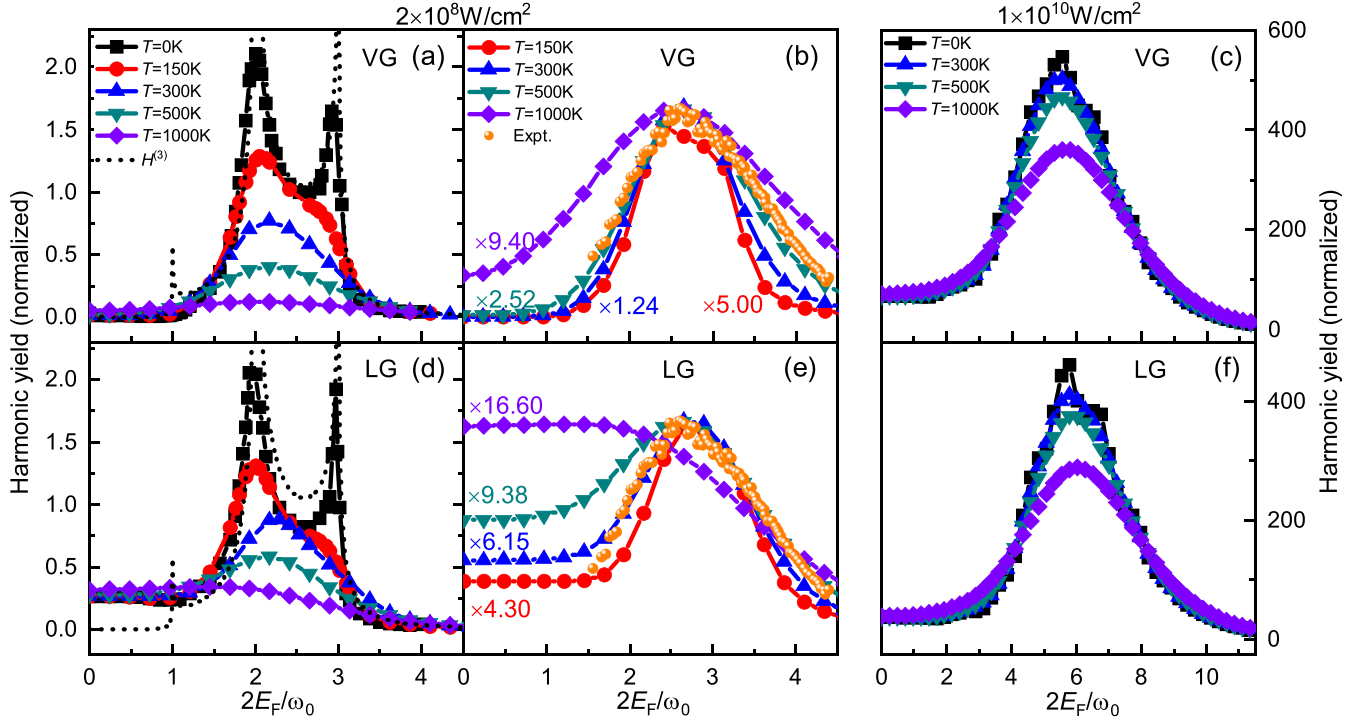


FIG. 6. Third harmonic yield as a function of Fermi energy  $E_F$  at different temperatures for  $2 \times 10^8$  W/cm<sup>2</sup> (a) in the perturbative region and  $1 \times 10^{10}$  W/cm<sup>2</sup> (c) in the plateau region. The dashed line in (a) presents the perturbation theory result of the third harmonic calculated by Eq. (B3). (b) Comparison between the experimental results of Ref. [56] and our numerical results for  $2 \times 10^8$  W/cm<sup>2</sup>, in which the relaxation parameters of  $\Gamma_i = 0$  and  $\Gamma_e = 0.002$  a.u. have been taken into account in the TBDMEs of the velocity gauge (VG). Panels (d), (e), and (f) are the same as (a), (b), and (c), respectively, but the results are calculated by the TBDMEs in the length gauge (LG). In panel (e), the dephasing time is set to be  $1/T_2 = 0.002$  atom unit.

According to Eq. (13), the yield peak of  $\tilde{H}(\omega_{cv}^M)$  arises from constructive quantum interference of  $\tilde{H}(\mathbf{k})$ .

Figure 5(d) shows that around  $\omega_{cv}^M$  (in the region of  $10\omega_0 < \omega_{cv} < 33.7\omega_0$  for  $1 \times 10^{12}$  W/cm<sup>2</sup>), the phases  $\tilde{\phi}(\omega_{cv})$  remain at  $-\pi/2$ . Equation (11) indicates that the constructive quantum interference of  $\tilde{H}(\omega_{cv})$  around  $\omega_{cv}^M$  can enhance the total harmonic yield  $\tilde{H}_{\text{tot}}$ .

The above picture is valid in the whole nonperturbative growth region. For instance, we extend the calculation to the third harmonic yields and phases for the higher intensity of  $1.1 \times 10^{12}$  W/cm<sup>2</sup>, as shown in Figs. 5(c) and 5(d). We also observe the effect of the constructive quantum interference of the Bloch electrons around  $M$  points. Quantitatively, with increasing laser intensity, the height and width of the dominating peak increase, which will lead to the nonperturbative growth of the third harmonic yield.

The above mechanism analysis is based on TBDMEs in the velocity gauge. For comparison, we also make extensive calculations and discussions based on TBDMEs of the length gauge, as shown in Appendix A.

### C. Effects of finite temperature and Fermi energy tuning

For a laser intensity of  $2 \times 10^8$  W/cm<sup>2</sup>, Fig. 6(a) shows that when the temperature is 0, the third harmonic yield significantly changes with increasing Fermi energy and a double-peak structure located at  $2E_F = 2\omega_0$  and  $2E_F = 3\omega_0$  is observed. This result agrees with the prediction from perturbation theory for graphene calculated by Eq. (B3), which

is represented by the dashed line. The effect of increasing the Fermi energy  $E_F$  on the third harmonic is caused by Pauli blocking. As the Fermi energy increases from  $E_F = 0$  to  $2E_F = 4\omega_0$ , one-photon, two-photon, and three-photon transitions are blocked in sequence. As the temperature increases, the double-peak structure is smoothed and evolves into a single-peak structure centered at  $2E_F = 2.17\omega_0$ .

When the temperature is set to 0, compared with  $E_F = 0$ , the third harmonic yield of doped graphene with  $2E_F = 2.17\omega_0$  is significantly enhanced. The influence of this Fermi energy tuning on the knee structure is clearly shown by the comparison between the black and red curves of Fig. 2(f). When the Fermi energy is 0, Fig. 6(a) shows that the third harmonic yields are not sensitive to temperature. When the Fermi energy is tuned to  $2E_F = 2.17\omega_0$ , the harmonic yield decreases with increasing temperature.

In Fig. 6(b), our numerical results in which the relaxation parameters of  $\Gamma_i = 0$  and  $\Gamma_e = 0.002$  a.u. (corresponding to a relaxation time of 12.1 fs) have been considered are compared with the experimental results of Ref. [56]. For four typical temperatures  $T = 150$  K, 300 K, 500 K, and 1000 K, the numerical results have been scaled by factors of 5.00, 1.24, 2.52, and 9.40, respectively. The numerical results for the temperature of 500 K match the experimental results, showing good agreement. Note that our extended calculations show that the results of Fig. 6(b) are almost independent of the laser intensity in the perturbative region.

For an intensity of  $1 \times 10^{10}$  W/cm<sup>2</sup> in the plateau region, the dependence of the third harmonic yield on the Fermi

energy exhibits a single-peak structure centered at  $2E_F = 5.5\omega_0$ , as shown in Fig. 6(c). Compared with the results for  $2 \times 10^8 \text{ W/cm}^2$ , the single-peak structure is more insensitive to temperature. More importantly, for temperature  $T = 0$ , the third harmonic yield of doped graphene with  $2E_F = 5.5\omega_0$  is tenfold stronger than that with  $E_F = 0$ . This result is also reflected in the comparison between the blue triangle curve and black square curve in Fig. 2(f), where the harmonic yield in the plateau region increases with the Fermi energy transition. At the same time, the harmonic yield in the perturbative region is obviously suppressed because of Pauli blocking. These results indicate that for the perturbative and plateau regions, tuning the Fermi energy can significantly influence the knee structure.

To verify these simulation results, we also perform TB-DME simulations of the length gauge and show the results in Figs. 6(d), 6(e) and 6(f). The results of the length gauge are qualitatively consistent with those of the velocity gauge. In contrast to Fig. 6(b), however, Fig. 6(e) shows that the numerical and experimental results are a better match at 300 K than at 500 K.

#### IV. CONCLUSION

In summary, we have investigated the harmonic generation of graphene irradiated by linearly polarized lasers with various intensities and found a striking knee structure, in contrast

to the atomic and molecular situations. The underlying mechanism is determined to be the destructive and constructive quantum interference of harmonics generated by the electrons corresponding to the lattice momenta around Dirac points and  $M$  points in the Brillouin zone, respectively. Our findings have also been confirmed by *ab initio* TDDFT calculations. In particular, we find that tuning the Fermi energy can effectively alter the knee structure, while the profile of the knee structure is not sensitive to temperature. The knee structure is rather universal and its associated properties can be observed with the current experimental techniques. In fact, our calculations of the third-order harmonic versus the tuned Fermi energy have been compared with a recent experiment, showing good agreement.

#### ACKNOWLEDGMENT

This work is supported by NSAF (Grant No. U1930403). We acknowledge valuable discussions with Prof. D. Ye.

#### APPENDIX A: COMPARISON OF THE RESULTS OF LENGTH AND VELOCITY GAUGES

##### 1. TBDMEs in the length gauge

We also calculate our main results by the TBDMEs of the length gauge [33]. Within the dipole approximation, they read

$$i \frac{\partial \rho_{cv}(\mathbf{k}, t)}{\partial t} = \left( E_{cv}(\mathbf{k}) - i \frac{1}{T_2} \right) \rho_{cv}(\mathbf{k}, t) + i \mathbf{E}(t) \cdot \nabla_{\mathbf{k}} \rho_{cv}(\mathbf{k}, t) + \mathbf{E}(t) \cdot [\mathbf{D}_{cv}(\mathbf{k}) \rho_{vv}(\mathbf{k}, t) - \rho_{cc}(\mathbf{k}, t) \mathbf{D}_{cv}(\mathbf{k})], \quad (\text{A1a})$$

$$i \frac{\partial \rho_{vv}(\mathbf{k}, t)}{\partial t} = \mathbf{E}(t) \cdot [\mathbf{D}_{vc}(\mathbf{k}) \rho_{cv}(\mathbf{k}, t) - \rho_{vc}(\mathbf{k}, t) \mathbf{D}_{cv}(\mathbf{k})] + i \mathbf{E}(t) \cdot \nabla_{\mathbf{k}} \rho_{vv}(\mathbf{k}, t), \quad (\text{A1b})$$

$$i \frac{\partial \rho_{cc}(\mathbf{k}, t)}{\partial t} = \mathbf{E}(t) \cdot [\mathbf{D}_{cv}(\mathbf{k}) \rho_{vc}(\mathbf{k}, t) - \rho_{cv}(\mathbf{k}, t) \mathbf{D}_{vc}(\mathbf{k})] + i \mathbf{E}(t) \cdot \nabla_{\mathbf{k}} \rho_{cc}(\mathbf{k}, t). \quad (\text{A1c})$$

At the initial moment  $t = 0$ , the assignment method of the density-matrix elements in the length gauge agrees with that of the velocity gauge.  $E_{cv}(\mathbf{k}) = E_c(\mathbf{k}) - E_v(\mathbf{k})$  is the band energy difference with lattice momentum  $\mathbf{k}$ . The interband dipole elements of the coordinate operator  $\mathbf{D}_{cv}(\mathbf{k})$  have been mentioned in the main text.  $T_2$  is the interband dephasing time.  $\mathbf{A}(t)$  is the vector potential of the laser field and  $\mathbf{E}(t) = -\partial \mathbf{A}(t)/\partial t$  is the electric field. The laser parameters of the length gauge are consistent with those of the velocity gauge.

The computational complexity introduced by the gradients in Eqs. (A1) can be removed by transforming the crystal momentum  $\mathbf{k}$  into a frame moving one  $\mathbf{k}_t = \mathbf{k} + \mathbf{A}(t)$  [61]. Under this transformation, the partial differential equations (A1) reduce to the following ordinary differential equations [21,62–64]:

$$i \frac{d \rho_{cv}(\mathbf{k}_t, t)}{dt} = \left( E_{cv}(\mathbf{k}_t) - i \frac{1}{T_2} \right) \rho_{cv}(\mathbf{k}_t, t) + \mathbf{E}(t) \cdot [\mathbf{D}_{cv}(\mathbf{k}_t) \rho_{vv}(\mathbf{k}_t, t) - \rho_{cc}(\mathbf{k}_t, t) \mathbf{D}_{cv}(\mathbf{k}_t)], \quad (\text{A2a})$$

$$i \frac{d \rho_{vv}(\mathbf{k}_t, t)}{dt} = \mathbf{E}(t) \cdot [\mathbf{D}_{vc}(\mathbf{k}_t) \rho_{cv}(\mathbf{k}_t, t) - \rho_{vc}(\mathbf{k}_t, t) \mathbf{D}_{cv}(\mathbf{k}_t)], \quad (\text{A2b})$$

$$i \frac{d \rho_{cc}(\mathbf{k}_t, t)}{dt} = \mathbf{E}(t) \cdot [\mathbf{D}_{cv}(\mathbf{k}_t) \rho_{vc}(\mathbf{k}_t, t) - \rho_{cv}(\mathbf{k}_t, t) \mathbf{D}_{vc}(\mathbf{k}_t)]. \quad (\text{A2c})$$

The above ordinary differential equations can be readily numerically solved by the standard fourth-order Runge-Kutta algorithm.

The total current can be evaluated by

$$\mathbf{j}_{\text{tot}}(t) = \sum_{\mathbf{k} \in \text{BZ}} \mathbf{j}(\mathbf{k}, t) = \sum_{\mathbf{k} \in \text{BZ}} [\mathbf{j}_{\text{inter}}(\mathbf{k}, t) + \mathbf{j}_{\text{intra}}(\mathbf{k}, t)] = \mathbf{j}_{\text{inter}}(t) + \mathbf{j}_{\text{intra}}(t), \quad (\text{A3})$$

where  $\mathbf{j}_{\text{inter}}(t)$  and  $\mathbf{j}_{\text{intra}}(t)$  are the interband and intraband currents, respectively. For each electron with lattice momentum  $\mathbf{k}$ , the interband and intraband currents can be calculated by

$$\mathbf{j}_{\text{inter}}(\mathbf{k}, t) = \mathbf{p}_{cv}(\mathbf{k}_t) \rho_{vc}(\mathbf{k}_t, t) + \mathbf{p}_{vc}(\mathbf{k}_t) \rho_{cv}(\mathbf{k}_t, t), \quad (\text{A4a})$$

$$\mathbf{j}_{\text{intra}}(\mathbf{k}, t) = \mathbf{p}_{cc}(\mathbf{k}_t) \rho_{cc}(\mathbf{k}_t, t) + \mathbf{p}_{vv}(\mathbf{k}_t) \rho_{vv}(\mathbf{k}_t, t), \quad (\text{A4b})$$



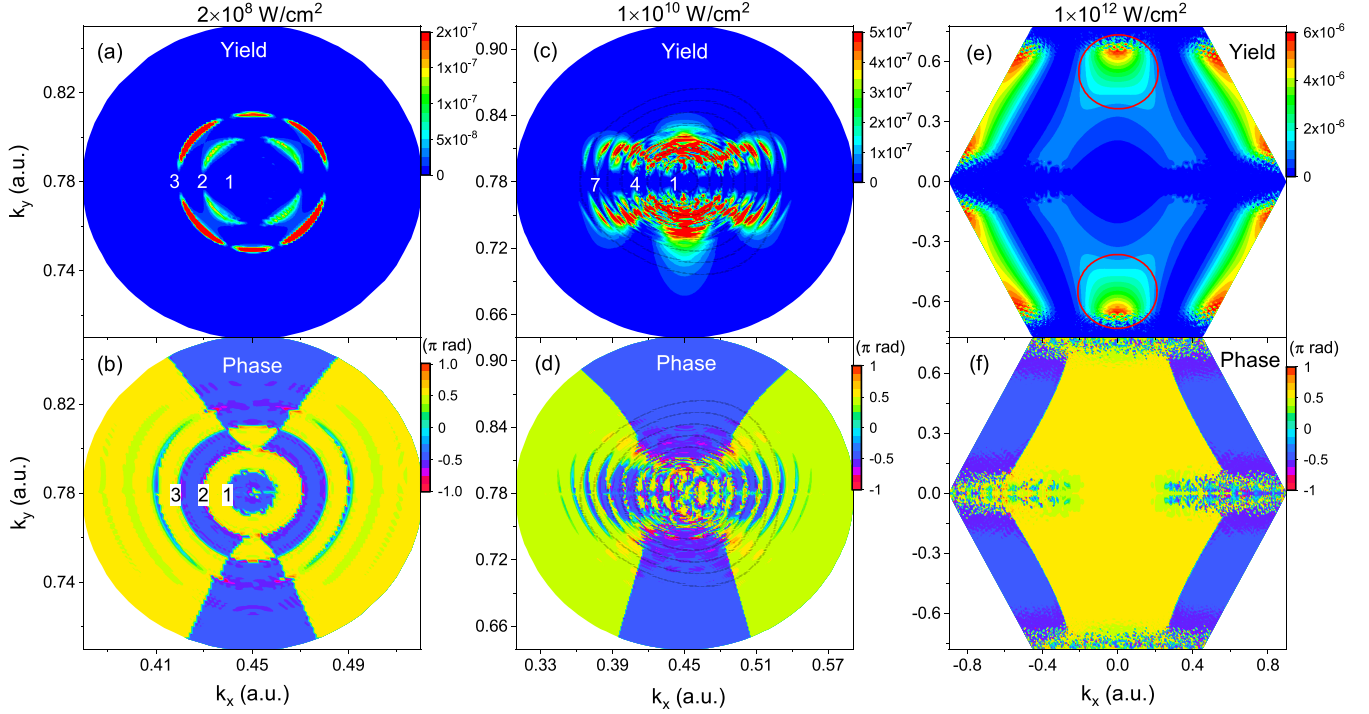


FIG. 7. For the laser intensities of  $2 \times 10^8 \text{ W/cm}^2$  [(a) and (b)] of the perturbative region,  $1 \times 10^{10} \text{ W/cm}^2$  [(c) and (d)] of the plateau region, and  $1 \times 10^{12} \text{ W/cm}^2$  [(e) and (f)] of the nonperturbative growth region, the yield  $\tilde{H}(\mathbf{k})$  [(a), (c), and (e)] and phase  $\tilde{\phi}(\mathbf{k})$  [(b), (d), and (f)]. Panels (a) and (b) [panels (c) and (d); panels (e) and (f)] are the same as Figs. 3(a) and 3(b) [Figs. 4(a) and 4(b); Figs. 5(a) and 5(b)], but the results are calculated by TBDMEs of the length gauge with  $1/T_2 = 0$ .

where the dipole elements of the momentum operator have been mentioned in the main text.

## 2. Third harmonic yield $\tilde{H}(\mathbf{k})$ and phase $\tilde{\phi}(\mathbf{k})$ as a function of lattice momentum $\mathbf{k}$ in the length gauge

On the basis of the TBDMEs of the length gauge, we also calculate the third harmonic yield  $\tilde{H}(\mathbf{k})$  and phase  $\tilde{\phi}(\mathbf{k})$ , as shown in Fig. 7. For  $2 \times 10^8 \text{ W/cm}^2$  of the perturbative region and  $1 \times 10^{10} \text{ W/cm}^2$  of the plateau region, the results of the length gauge shown in Fig. 7 agree with those of the velocity gauge presented in the main text.

For a laser intensity  $1 \times 10^{12} \text{ W/cm}^2$  of the nonperturbative growth region, the yields of the length gauge shown in Fig. 7(e) do not exactly agree with those of the velocity gauge presented in Fig. 5(a). The main difference is that for the lattice momenta inside the red circles, the harmonic yields  $\tilde{H}(\mathbf{k})$  of the length gauge [Fig. 7(e)] are larger than those of the velocity gauge [Fig. 5(a)]. The corresponding phases  $\tilde{\phi}(\mathbf{k})$  are  $\pi/2$  as shown in Fig. 7(f). Note that the harmonic phases near the  $M$  points are  $-\pi/2$ . The phase difference of  $\pi$  can cause destructive interference of the harmonics according to Eq. (10). Thus the total harmonic yield of the nonperturbative growth region for the length gauge is smaller than that of the velocity gauge, as shown in Fig. 2(d).

For the effect of the temperature and tuning the Fermi energy on the knee structure shown in Figs. 2(d) and 2(f), which are mainly associated with the perturbative and plateau regions, the results based on the length gauge are consistent

with those of the velocity gauge according to our further calculations.

## 3. Discontinuous phase distribution

In Figs. 7(b), 7(d) and 7(f), as well as the velocity gauge counterparts of Figs. 3(b), 4(b) and 5(b), we find discontinuous phase distributions. The interesting  $\pi$ -phase jumps in Fig. 5(d) also originate from the phase distribution. In the following discussion, taking the nonperturbative growth region as an example, we address the mechanism for the discontinuous phase distribution.

In the nonperturbative growth region, our calculations indicate that the intraband dynamics dominate the third harmonic generation. In the length gauge, a lattice momentum  $\mathbf{k} = (k_x, k_y)$  is transformed to  $\mathbf{k} + \mathbf{A}(t) = [k_x + A(t), k_y]$ . The intraband current of the electron with lattice momentum  $\mathbf{k}$  is given by  $j_{\text{intra}}(\mathbf{k}, t) \propto \partial E_c(p, k_y)/\partial p|_{p=k_x+A(t)}$  [65], where we set  $A(t) = A_0 \sin(\omega_0 t)$  for simplicity. One can obtain  $\tilde{F}_{\text{intra}}(\mathbf{k}) = \frac{\omega_0}{\pi} \int_{-\pi/\omega_0}^{\pi/\omega_0} j_{\text{intra}}(\mathbf{k}, t) e^{-i3\omega_0 t} dt$ . Considering the symmetry associated with the concrete expression of the energy band  $E_c(k_x, k_y)$ , mathematically, we can prove that the real part  $\text{Re}[\tilde{F}_{\text{intra}}(\mathbf{k})]$  is always zero. Then the phase of the third harmonic  $\tilde{\phi}_{\text{intra}}(\mathbf{k}) = \arctan \frac{\text{Im}[\tilde{F}_{\text{intra}}(\mathbf{k})]}{\text{Re}[\tilde{F}_{\text{intra}}(\mathbf{k})]} = \pm\pi/2$ . The “ $\pm$ ” sign depends on the sign of the nonzero imaginary part and therefore is related to the corresponding lattice momentum  $\mathbf{k}$ .

In the above discussions, we ignore the interband transitions. Near the  $K$  points in the Brillouin zone, tunneling

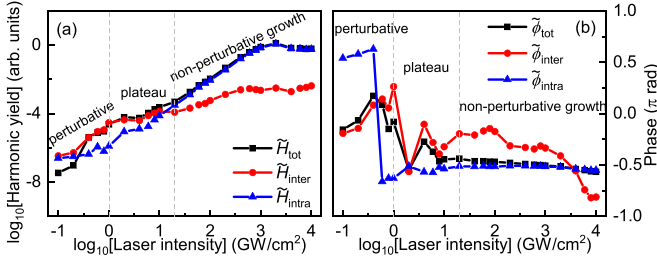


FIG. 8. Laser intensity dependence of the third harmonic yields (a) and phases (b), which are calculated by the TBDMEs of Eqs. (A2). Here, the dephasing time is set to  $1/T_2 = 0$  and the laser wavelength is 5500 nm.

between the two energy bands is important and might complicate the electron motion and lead to an irregular phase distribution, as shown in Fig. 7(f).

#### 4. Mechanism analysis of the knee structure in the length gauge

We also study the effect of the interband and intraband dynamics on the knee structure under the length gauge. Equation (A3) tells us that the total current is the sum of the interband and intraband currents, i.e.,  $\tilde{j}_{\text{tot}}(t) = \tilde{j}_{\text{inter}}(t) + \tilde{j}_{\text{intra}}(t)$ . One can obtain

$$\sqrt{\tilde{H}_{\text{tot}}} \cdot e^{i\tilde{\phi}_{\text{tot}}} = \sqrt{\tilde{H}_{\text{inter}}} \cdot e^{i\tilde{\phi}_{\text{inter}}} + \sqrt{\tilde{H}_{\text{intra}}} \cdot e^{i\tilde{\phi}_{\text{intra}}}, \quad (\text{A5})$$

where  $\tilde{H}_{\text{tot}} \equiv H_{\text{tot}}(3\omega_0) = (3\omega_0)^2 |\tilde{F}_{\text{tot}}|^2$ . The corresponding phase  $\tilde{\phi}_{\text{tot}} = \arg(\tilde{F}_{\text{tot}}) \in [-\pi, \pi)$  is calculated by considering  $\tan[\tilde{\phi}_{\text{tot}}] = \text{Im}[\tilde{F}_{\text{tot}}] / \text{Re}[\tilde{F}_{\text{tot}}]$ , in which  $\tilde{F}_{\text{tot}} = \int_{-\infty}^{\infty} \mathbf{e} \cdot \tilde{j}_{\text{tot}}(t) e^{-i3\omega_0 t} dt$ . The third interband (or intraband) harmonic yield  $\tilde{H}_{\text{inter}}$  (or  $\tilde{H}_{\text{intra}}$ ) and phase  $\tilde{\phi}_{\text{inter}}$  (or  $\tilde{\phi}_{\text{intra}}$ ) can be calculated with the interband current  $\tilde{j}_{\text{inter}}(t)$  [or intraband current  $\tilde{j}_{\text{intra}}(t)$ ] by the same formulas.

We show the laser intensity dependence of the third harmonic yields ( $\tilde{H}_{\text{tot}}$ ,  $\tilde{H}_{\text{inter}}$ ,  $\tilde{H}_{\text{intra}}$ ) and phases ( $\tilde{\phi}_{\text{tot}}$ ,  $\tilde{\phi}_{\text{inter}}$ ,  $\tilde{\phi}_{\text{intra}}$ ) in Fig. 8. In the perturbative region, as the laser intensity increases,  $\tilde{H}_{\text{tot}}$  and  $\tilde{H}_{\text{inter}}$  increase rapidly, while  $\tilde{H}_{\text{intra}}$  remains stable [see Fig. 8(a)]. Figure 8(b) shows that the phases  $\tilde{\phi}_{\text{tot}}$  are close to  $\tilde{\phi}_{\text{inter}}$  in this region. One can conclude that the rapid increase in  $\tilde{H}_{\text{tot}}$  is caused by the increase in  $\tilde{H}_{\text{inter}}$ . The underlying mechanism is that in the perturbative region, a few electrons near Dirac points can be excited and the trajectories of these electrons are short in the reciprocal space due to small vector potential. Therefore, the third harmonic generation is dominated by the multiphoton transitions instead of the intraband dynamics.

In contrast to the perturbative region, in the plateau region, the intraband yield  $\tilde{H}_{\text{intra}}$  increases rapidly, unlike the interband yield  $\tilde{H}_{\text{inter}}$ . A transition from  $\tilde{H}_{\text{inter}} > \tilde{H}_{\text{intra}}$  to  $\tilde{H}_{\text{inter}} < \tilde{H}_{\text{intra}}$  appears in this region, which suppresses the rapid growth of  $\tilde{H}_{\text{tot}}$ . On the other hand, one can find that the interband yields  $\tilde{H}_{\text{inter}}$  are comparable to the intraband yields  $\tilde{H}_{\text{intra}}$  on the whole and there exist phase differences between  $\tilde{\phi}_{\text{inter}}$  and  $\tilde{\phi}_{\text{intra}}$ . According to Eq. (A5), the interference between  $\tilde{H}_{\text{inter}}$  and  $\tilde{H}_{\text{intra}}$  also suppresses the rapid increase in  $\tilde{H}_{\text{tot}}$  in the plateau region.

In the nonperturbative growth region, with increasing laser intensity, the intraband yield  $\tilde{H}_{\text{intra}}$  first increases rapidly

(from  $2 \times 10^{10}$  W/cm<sup>2</sup> to  $2 \times 10^{12}$  W/cm<sup>2</sup>) and then remains stable (from  $2 \times 10^{12}$  W/cm<sup>2</sup> to  $1 \times 10^{13}$  W/cm<sup>2</sup>), while the interband yield  $\tilde{H}_{\text{inter}}$  slowly increases. Because the intraband yields  $\tilde{H}_{\text{intra}}$  are much larger than the interband yields  $\tilde{H}_{\text{inter}}$ , according to Eq. (A5), the phases  $\tilde{\phi}_{\text{tot}}$  are close to the intraband phases  $\tilde{\phi}_{\text{intra}}$  [see Fig. 8(b)]. Therefore, in the nonperturbative growth region, the rapid increase in  $\tilde{H}_{\text{tot}}$  originates from the increase in  $\tilde{H}_{\text{intra}}$ . The underlying mechanism is that as the laser intensity increases, more electrons near  $M$  points can be excited, and the trajectories of the excited electrons are longer in the reciprocal space with the increase of the vector potential. Therefore, the intraband dynamics of those electrons play a key role in the third harmonic generation.

#### APPENDIX B: PERTURBATION THEORY

Within the perturbation theory framework [34,60], the current of graphene can be calculated by  $J(t) = \sum_{n=1}^{\infty} J^{(n)}(t)$ , where  $J^{(n)}(t)$  is the  $n$ th-order perturbation expansion of the current. For doped graphene with Fermi energy  $E_F$  (here, we have set  $E_F \geq 0$ ), the time-dependent third-order current is given as

$$J^{(3)}(E_F, t) = \int d\omega \sigma^{(3)}(E_F, \omega) E^3(\omega) e^{-i3\omega t}, \quad (\text{B1})$$

where  $\sigma^{(3)}$  is the third-order optical conductivity and  $E(\omega)$  is the Fourier transform of electric field  $E(t)$ .

To simplify, we consider the electric field  $E(t) = E_0 \cos(\omega_0 t)$  and therefore Eq. (B1) can be simplified to

$$J^{(3)}(E_F, t) = \sigma^{(3)}(E_F, \omega_0) E_0^3 e^{-i3\omega_0 t}, \quad (\text{B2})$$

in which  $\sigma^{(3)}(E_F, \omega_0) \propto i \frac{1}{\omega_0} T\left(\frac{\omega_0}{2E_F}\right)$  [60].

The third harmonic yield of doped graphene with Fermi energy  $E_F$  is evaluated by

$$\begin{aligned} H^{(3)}(E_F) &= (3\omega_0)^2 |\mathcal{T}_F[J^{(3)}(E_F, t)]|^2 \\ &= (3\omega_0)^2 |\sigma^{(3)}(E_F, \omega_0)|^2 E_0^6 \propto \frac{9I^3}{\omega_0^6} \left| T\left(\frac{\omega_0}{2E_F}\right) \right|^2, \end{aligned} \quad (\text{B3})$$

where  $T(x) = 17G(x) - 64G(2x) + 45G(3x)$ , in which

$$G(x) = \ln \left| \frac{1+x}{1-x} \right| + i\pi\theta(|x|-1) \quad (\text{B4})$$

is a dimensionless complex function of a real variable  $x$ . Here,  $\theta(y)$  is the Heaviside step function, equal to 0 for  $y < 0$  and 1 for  $y > 0$ .

On the other hand, the third-order term of the current  $j(\omega_{cv}, t)$  can be evaluated by

$$\begin{aligned} j^{(3)}(\omega_{cv}, t) &= \lim_{\Delta\varepsilon \rightarrow 0} J^{(3)}(\omega_{cv}/2 - \Delta\varepsilon, t) \\ &\quad - \lim_{\Delta\varepsilon \rightarrow 0} J^{(3)}(\omega_{cv}/2 + \Delta\varepsilon, t), \end{aligned} \quad (\text{B5})$$

where  $J^{(3)}(\mu, t)$  is the third-order current for doped graphene with Fermi energy  $E_F = \mu$  as mentioned by Eq. (B2). The third harmonic yield as a function of the band frequency

difference  $\omega_{cv}$  is evaluated by

$$\tilde{H}(\omega_{cv}) = (3\omega_0)^2 |\tilde{F}(\omega_{cv})|^2 \propto (3\omega_0)^2 I^3 \left| \lim_{\Delta\varepsilon \rightarrow 0} [\sigma^{(3)}(\omega_{cv}/2 - \Delta\varepsilon, \omega_0) - \sigma^{(3)}(\omega_{cv}/2 + \Delta\varepsilon, \omega_0)] \right|^2, \quad (\text{B6})$$

where we have used  $\tilde{F}(\omega_{cv}) = \mathcal{T}_F[j^{(3)}(\omega_{cv}, t)]$ . The phase  $\tilde{\phi}(\omega_{cv})$  is calculated by

$$\tan[\tilde{\phi}(\omega_{cv})] = \text{Im}[\tilde{F}(\omega_{cv})] / \text{Re}[\tilde{F}(\omega_{cv})]. \quad (\text{B7})$$

- 
- [1] P. B. Corkum, Plasma Perspective on Strong Field Multiphoton Ionization, *Phys. Rev. Lett.* **71**, 1994 (1993).
- [2] M. Lewenstein, Ph. Balcou, M. Yu. Ivanov, A. L’Huillier, and P. B. Corkum, Theory of high-harmonic generation by low-frequency laser fields, *Phys. Rev. A* **49**, 2117 (1994).
- [3] J. Itatani, J. Levesque, D. Zeidler, H. Niikura, H. Pépin, J. C. Kieffer, P. B. Corkum, and D. M. Villeneuve, Tomographic imaging of molecular orbitals, *Nature (London)* **432**, 867 (2004).
- [4] M. Meckel, D. Comtois, D. Zeidler, A. Staudte, D. Pavičić, H. C. Bandulet, H. Pépin, J. C. Kieffer, R. Dörner, D. M. Villeneuve, and P. B. Corkum, Laser-induced electron tunneling and diffraction, *Science* **320**, 1478 (2008).
- [5] F. Krausz and M. Ivanov, Attosecond physics, *Rev. Mod. Phys.* **81**, 163 (2009).
- [6] T. T. Luu, M. Garg, S. Yu. Kruchinin, A. Moulet, M. Th. Hassan, and E. Goulielmakis, Extreme ultraviolet high-harmonic spectroscopy of solids, *Nature (London)* **521**, 498 (2015).
- [7] S. Ghimire, A. D. DiChiara, E. Sistrunk, P. Agostini, L. F. DiMauro, and D. A. Reis, Observation of high-order harmonic generation in a bulk crystal, *Nat. Phys.* **7**, 138 (2011).
- [8] G. Vampa, T. J. Hammond, N. Thiré, B. E. Schmidt, F. Légaré, C. R. McDonald, T. Brabec, D. D. Klug, and P. B. Corkum, All-Optical Reconstruction of Crystal Band Structure, *Phys. Rev. Lett.* **115**, 193603 (2015).
- [9] A. Lanin, E. Stepanov, A. Fedotov, and A. Zheltikov, Mapping the electron band structure by intraband high-harmonic generation in solids, *Optica* **4**, 516 (2017).
- [10] M. Garg, M. Zhan, T. T. Luu, H. Lakhota, T. Klostermann, A. Guggenmos, and E. Goulielmakis, Multi-petahertz electronic metrology, *Nature (London)* **538**, 359 (2016).
- [11] A. H. Castro Neto, F. Guinea, N. M. R. Peres, K. S. Novoselov, and A. K. Geim, The electronic properties of graphene, *Rev. Mod. Phys.* **81**, 109 (2009).
- [12] N. Yoshikawa, T. Tamaya, and K. Tanaka, High-harmonic generation in graphene enhanced by elliptically polarized light excitation, *Science* **356**, 736 (2017).
- [13] J. D. Cox, A. Marini, and F. J. García de Abajo, Plasmon-assisted high-harmonic generation in graphene, *Nat. Commun.* **8**, 14380 (2017).
- [14] Z. Chen and R. Qin, Circularly polarized extreme ultraviolet high harmonic generation in graphene, *Opt. Express* **27**, 3761 (2019).
- [15] Y. Zhang, L. Li, J. Li, T. Huang, P. Lan, and P. Lu, Orientation dependence of high-order harmonic generation in graphene, *Phys. Rev. A* **104**, 033110 (2021).
- [16] C. Liu, Y. Zheng, Z. Zeng, and R. Li, Driving-laser ellipticity dependence of high-order harmonic generation in graphene, *Phys. Rev. A* **97**, 063412 (2018).
- [17] Y. Feng, S. Shi, J. Li, Y. Ren, X. Zhang, J. Chen, and H. Du, Semiclassical analysis of ellipticity dependence of harmonic yield in graphene, *Phys. Rev. A* **104**, 043525 (2021).
- [18] S. A. Sato, H. Hirori, Y. Sanari, Y. Kanemitsu, and A. Rubio, High-order harmonic generation in graphene: Nonlinear coupling of intraband and interband transitions, *Phys. Rev. B* **103**, L041408 (2021).
- [19] O. Zurrón-Cifuentes, R. Boyero-García, C. Hernández-García, A. Picón, and L. Plaja, Optical anisotropy of non-perturbative high-order harmonic generation in gapless graphene, *Opt. Express* **27**, 7776 (2019).
- [20] F. Dong, Q. Xia, and J. Liu, Ellipticity of the harmonic emission from graphene irradiated by a linearly polarized laser, *Phys. Rev. A* **104**, 033119 (2021).
- [21] M. S. Mrudul and G. Dixit, High-harmonic generation from monolayer and bilayer graphene, *Phys. Rev. B* **103**, 094308 (2021).
- [22] M. Du, C. Liu, Z. Zeng, and R. Li, High-order harmonic generation from twisted bilayer graphene driven by a midinfrared laser field, *Phys. Rev. A* **104**, 033113 (2021).
- [23] J. Liu, *Classical Trajectory Perspective of Atomic Ionization in Strong Laser Fields* (Springer, Heidelberg, 2014).
- [24] B. Walker, B. Sheehy, L. F. DiMauro, P. Agostini, K. J. Schafer, and K. C. Kulander, Precision Measurement of Strong Field Double Ionization of Helium, *Phys. Rev. Lett.* **73**, 1227 (1994).
- [25] C. Guo, M. Li, J. P. Nibarger, and G. N. Gibson, Single and double ionization of diatomic molecules in strong laser fields, *Phys. Rev. A* **58**, R4271 (1998).
- [26] C. Cornaggia and Ph. Hering, Nonsequential double ionization of small molecules induced by a femtosecond laser field, *Phys. Rev. A* **62**, 023403 (2000).
- [27] Y. H. Lai, J. Xu, U. B. Szafruga, B. K. Talbert, X. Gong, K. Zhang, H. Fuest, M. F. Kling, C. I. Blaga, P. Agostini, and L. F. DiMauro, Experimental investigation of strong-field-ionization theories for laser fields from visible to midinfrared frequencies, *Phys. Rev. A* **96**, 063417 (2017).
- [28] C.-G. Wahlström, J. Larsson, A. Persson, T. Starczewski, S. Svanberg, P. Salieres, Ph. Balcou, and A. L’Huillier, High-order harmonic generation in rare gases with an intense short-pulse laser, *Phys. Rev. A* **48**, 4709 (1993).
- [29] L. A. Lompré, A. L’Huillier, M. Ferray, P. Monot, G. Mainfray, and C. Manus, High-order harmonic generation in xenon: Intensity and propagation effects, *J. Opt. Soc. Am. B* **7**, 754 (1990).
- [30] K. Amiri *et al.*, Symphony on strong field approximation, *Rep. Prog. Phys.* **82**, 116001 (2019).
- [31] P. R. Wallace, The band theory of graphite, *Phys. Rev.* **71**, 622 (1947).
- [32] G. Vampa, C. R. McDonald, G. Orlando, D. D. Klug, P. B. Corkum, and T. Brabec, Theoretical Analysis of

- High-Harmonic Generation in Solids, *Phys. Rev. Lett.* **113**, 073901 (2014).
- [33] S. C. Jiang, H. Wei, J. G. Chen, C. Yu, R. F. Lu, and C. D. Lin, Effect of transition dipole phase on high-order-harmonic generation in solid materials, *Phys. Rev. A* **96**, 053850 (2017).
- [34] J. L. Cheng, N. Vermeulen, and J. E. Sipe, Third-order nonlinearity of graphene: Effects of phenomenological relaxation and finite temperature, *Phys. Rev. B* **91**, 235320 (2015).
- [35] C. A. Ullrich, *Time-Dependent Density-Functional Theory: Concepts and Applications* (Oxford University Press, Oxford, 2011).
- [36] M. Marques and E. Gross, Time-dependent density functional theory, *Annu. Rev. Phys. Chem.* **55**, 427 (2004).
- [37] Z. Nourbakhsh, N. Tancogne-Dejean, H. Merdji, and A. Rubio, High harmonics and isolated attosecond pulses from MgO, *Phys. Rev. Appl.* **15**, 014013 (2021).
- [38] G. Le Breton, A. Rubio, and N. Tancogne-Dejean, High-harmonic generation from few-layer hexagonal boron nitride: Evolution from monolayer to bulk response, *Phys. Rev. B* **98**, 165308 (2018).
- [39] T. J. Giese and D. M. York, Density-functional expansion methods: evaluation of LDA, GGA, and meta-GGA functionals and different integral approximations, *J. Chem. Phys.* **133**, 244107 (2010).
- [40] A. J. Cohen, P. Mori-Sánchez, and W. Yang, Challenges for density functional theory, *Chem. Rev.* **112**, 289 (2012).
- [41] A. J. Cohen, P. Mori-Sánchez, and W. Yang, Insights into current limitations of density functional theory, *Science* **321**, 792 (2008).
- [42] X. Andrade, D. A. Strubbe, U. D. Giovannini, A. H. Larsen, M. J. T. Oliveira, J. Alberdi-Rodriguez, A. Varas, I. Theophilou, N. Helbig, M. Verstraete, L. Stella, F. Nogueira, A. Aspuru-Guzik, A. Castro, M. A. L. Marques, and A. Rubio, Real-space grids and the octopus code as tools for the development of new simulation approaches for electronic systems, *Phys. Chem. Chem. Phys.* **17**, 31371 (2015).
- [43] A. Castro, M. A. L. Marques, and A. Rubio, Propagators for the time-dependent Kohn-Sham equations, *J. Chem. Phys.* **121**, 3425 (2004).
- [44] W. E. Lamb, R. R. Schlicher, and M. O. Scully, Matter-field interaction in atomic physics and quantum optics, *Phys. Rev. A* **36**, 2763 (1987).
- [45] M. Scully and M. Zubairy, *Quantum Optics* (Cambridge University Press, Cambridge, UK, 1997).
- [46] V. S. Yakovlev and M. S. Wismer, Adiabatic corrections for velocity-gauge simulations of electron dynamics in periodic potentials, *Comput. Phys. Commun.* **217**, 82 (2017).
- [47] M. D. Feit, Jr., J. A. Fleck, Jr., and A. Steiger, Solution of the Schrödinger equation by a spectral method, *J. Comput. Phys.* **47**, 412 (1982).
- [48] In our work, the one-dimensional time-dependent Schrödinger equation of the model atom in the length gauge is numerically solved by the spectral method [47]. Here, we use the soft-Coulomb potential  $V(x) = -Z/\sqrt{\varepsilon + x^2}$  and set the effective charge  $Z = 0.172$  atomic units as well as the smoothing parameter  $\varepsilon = 0.5$  to ensure that the ionization potential of the model atom is 0.1 atomic units, which is comparable to the energy of the valence band of graphene. Additionally, the frequency of the electric field we use is 0.057 atomic units.
- [49] P. Xia, C. Kim, F. Lu, T. Kanai, H. Akiyama, J. Itatani, and N. Ishii, Nonlinear propagation effects in high harmonic generation in reflection and transmission from gallium arsenide, *Opt. Express* **26**, 29393 (2018).
- [50] H. Z. Liu, Y. L. Li, Y. S. You, S. Ghimire, T. F. Heinz, and D. A. Reis, High-harmonic generation from an atomically thin semiconductor, *Nat. Phys.* **13**, 262 (2017).
- [51] L. Li, T. Huang, P. Lan, J. Li, Y. Zhang, X. Zhu, L. He, W. Cao, and P. Lu, Fingerprint of the Interbond Electron Hopping in Second-Order Harmonic Generation, *Phys. Rev. Lett.* **128**, 027401 (2022).
- [52] A. Roberts, D. Cormode, C. Reynolds, T. N. Illige, B. J. LeRoy, and A. S. Sandhu, Response of graphene to femtosecond high-intensity laser irradiation, *Appl. Phys. Lett.* **99**, 051912 (2011).
- [53] H. Jeschke, M. Garcia, and K. H. Bennemann, Theory for the Ultrafast Ablation of Graphite Films, *Phys. Rev. Lett.* **87**, 015003 (2001).
- [54] F. Wang, Y. Zhang, C. Tian, C. Girit, A. Zettl, M. Crommie, and Y. R. Shen, Gate-variable optical transitions in graphene, *Science* **320**, 206 (2008).
- [55] F. H. Koppens, D. E. Chang, and F. J. García de Abajo, Graphene plasmonics: A platform for strong light-matter interactions, *Nano Lett.* **11**, 3370 (2011).
- [56] I. Alonso Calafell, L. A. Rozema, D. A. Iranzo, A. Trenti, P. K. Jenke, J. D. Cox, A. Kumar, H. Bieliaiev, S. Nanot, C. Peng, D. K. Efetov, J.-Y. Hong, J. Kong, D. R. Englund, F. J. García de Abajo, F. H. L. Koppens, and P. Walther, Giant enhancement of third-harmonic generation in graphene-metal heterostructures, *Nat. Nanotechnol.* **16**, 318 (2021).
- [57] T. Jiang, D. Huang, J. Cheng, X. Fan, Z. Zhang, Y. Shan, Y. Yi, Y. Dai, L. Shi, K. Liu, C. Zeng, J. Zi, J. E. Sipe, Y.-R. Shen, W.-T. Liu, and S. Wu, Gate-tunable third-order nonlinear optical response of massless Dirac fermions in graphene, *Nat. Photon.* **12**, 430 (2018).
- [58] G. Soavi, G. Wang, H. Rostami, D. G. Purdie, D. D. Fazio, T. Ma, B. Luo, J. Wang, A. K. Ott, D. Yoon, S. A. Borelle, J. E. Muench, I. Goykhman, S. D. Conte, M. Celebrano, A. Tomadin, M. Polini, G. Cerullo, and A. C. Ferrari, Broadband, electrically tunable third-harmonic generation in graphene, *Nat. Nanotechnol.* **13**, 583 (2018).
- [59] R. W. Boyd, *Nonlinear Optics*, 3rd ed. (Academic Press, Burlington, 2008).
- [60] J. L. Cheng, N. Vermeulen, and J. E. Sipe, Third order optical nonlinearity of graphene, *New J. Phys.* **16**, 053014 (2014).
- [61] W. V. Houston, Acceleration of electrons in a crystal lattice, *Phys. Rev.* **57**, 184 (1940).
- [62] H. K. Kelardeh, V. Apalkov, and M. I. Stockman, Wannier-Stark states of graphene in strong electric field, *Phys. Rev. B* **90**, 085313 (2014).
- [63] Ó. Zurrón, A. Picón, and L. Plaja, Theory of high-order harmonic generation for gapless graphene, *New J. Phys.* **20**, 053033 (2018).
- [64] H. K. Kelardeh, U. Saalman, and J. M. Rost, Ultrashort laser-driven dynamics of massless Dirac electrons generating valley polarization in graphene, *Phys. Rev. Res.* **4**, L022014 (2022).
- [65] F. Catoire, H. Bachau, Z. Wang, C. Blaga, P. Agostini, and L. F. DiMauro, Wannier Representation of Intraband High-Order Harmonic Generation, *Phys. Rev. Lett.* **121**, 143902 (2018).